Comparative annealing effect on bonded wafers in air and ultrahigh vacuum for microelectromechanical systems/microfluidics packaging

Matiar M. R. Howlader
McMaster University
Department of Electrical and Computer Engineering
Hamilton, Ontario L8S 4K1, Canada

Tadatomo Suga
University of Tokyo
Department of Precision Engineering
Tokyo 113-8656, Japan

Abstract. The fundamentals of room temperature bonding methods—surface activated bonding (SAB) and sequentially plasma-activated bonding (SPAB)—are reviewed with applications for packaging of microelectromechanical systems (MEMS) and microfluidic devices. The room temperature bonding strength of the silicon/silicon interface in the SAB and SPAB is as high as that of the hydrophilic bonding method, which requires annealing as high as 1000°C to achieve covalent bonding. After heating, voids are not observed and bonding strengths are not changed in the SAB. In the SPAB, interfacial voids are increased and decreased the bonding strength. Water rearrangement such as absorption and desorption across the bonded interface is found below 225°C. While voids are not significant up to 400°C, a considerable amount of thermal voids above 600°C is found due to viscous flow of oxides. Before heating, interfacial amorphous layers are observed both in the SAB (8.3 nm) and SPAB (4.8 nm), but after heating these disappear and enlarge in the SAB and SPAB, respectively. This enlarged amorphous layer is SiO_2, which is due to the oxidation of silicon/silicon interface after sequential heating. The bonding strength, sealing, and chemical performances of the interfaces meet the requirements for MEMS and microfluidics applications. © *2010 Society of Photo-Optical Instrumentation Engineers.* [DOI: 10.1117/1.3500747]

Subject terms: sequential plasma activated bonding; bonding strength; void; viscous flow; nanointerface; electron energy loss spectroscopy; sealing; chemical performance.

Paper 10013SSPR received Mar. 2, 2010; revised manuscript received Aug. 18, 2010; accepted for publication Aug. 26, 2010; published online Oct. 00, 2010.

1 Introduction

Packaging often appears as a limiting factor when moving research and design concepts to working prototypes such as microelectromechanical systems (MEMS). Room temperature direct bonding for MEMS and microfluidic devices packaging is now regarded as enabling technologies that are applicable to a large variety of MEMS projects and structures, and for demonstrating novel packaging. Since the bonding process is often the last step of packaging processes for MEMS devices, high temperature processing for bonding is not possible at that stage because of thermal mismatch problems and gas formation in the cavities that degrade device performance. MEMS devices are interfaced with real-world systems and respond to incoming signals.[1,2] In addition, many MEMS devices such as resonators, accelerometers, etc., require hermetic vacuum sealing or controllable cavity pressure[3] to protect them from harsh environments, internal gases, mechanical damage, and contaminations. Furthermore, MEMS devices may require no-load or low-load bonding methods because of the delicate nature of their structure.[4,5] Finally, it is well known that the packaging cost is about 70% of the total fabrication cost for devices, which can be reduced by wafer-level packaging.[6] Therefore, there is a significant demand for low temperature wafer-level bonding techniques for MEMS packaging.

Two room temperature surface-activation-based bonding methods, surface activated bonding (SAB) and sequential plasma activated bonding (SPAB), have been demonstrated for packaging of MEMS, microfluidic, and optoelectronic devices.[7] In the SAB method, two smooth surfaces are cleaned by using an argon fast atom beam (Ar-FAB) in an ultrahigh vacuum (UHV), followed by contact in vacuum. The SPAB combines the physical sputtering effect of reactive ion etching (RIE) plasma with the chemical reactivity of microwave (MW) radicals. Two activated wafers are contacted in air. Figure 1 shows the schematic diagram of the SAB and SPAB methods. In the SAB, the strong adhesion between two mated surfaces occurs because of the clean, smooth, and activated surfaces treated with Ar-FAB. In SPAB, spontaneous bonding occurs because of the concurrent removing of surface contaminants and native oxides, and depositing of oxides or nitrides on the activated surfaces. This process provides a high reactive surface that allows spontaneous bonding at room temperature.[8] The SAB and SPAB methods both offer a high bonding strength equivalent to that of bulk materials without annealing.

One of the issues with the bonding methods is the voids or unbonded regions at the interface. Voids control the reliability of the bonded interface such as bonding strength and hermeticity. Voids mainly attribute to the presence of surface particles, contaminants (i.e., hydrocarbon and metal ions from tweezers), reaction byproducts (i.e., H_2O and H_2), and plasma-induced defects. Nucleation of voids can

1932-5150/2010/$25.00 © 2010 SPIE

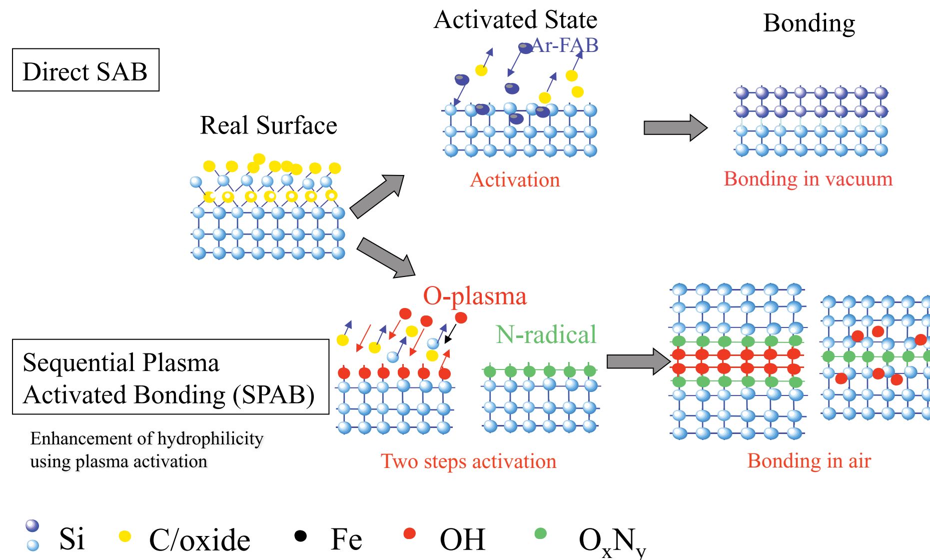

Fig. 1 Schematic diagram of surface-activated bonding (SAB) and sequential plasma-activated bonding (SPAB) methods. In both methods, high bonding strength is achieved without heating. In SAB, dangling sites of the activated surfaces adhere to each other. In SPAB, high reactive hydrophilic surfaces are strong at room temperature.

accelerate during the fabrication process flow at higher temperatures in some applications. For example, in smart-cut processes to fabricate silicon-on-insulator (SOI) substrates, ion-implanted and bonded specimens go through a high temperature annealing step, which is required for layer transfer.[9] Hence, study on the nucleation of voids at the bonded interface with different processing conditions such as plasma parameters, annealing environment, and temperature is needed.

Previously the sequentially plasma-activated silicon bonded wafers showed that the bonding strengths were reduced after annealing in air.[10] The cause of the reduction of the bonding strength was believed due to the formation of voids and brittle oxide layers across the interface. While the quality (i.e., tensile strength) of the bonded interface was investigated after annealing, the cause of the reduction of bonding strength after annealing was not investigated in terms of the void nucleation at the interface. On the other hand, the void nucleation as well as its relationship with the bonding strength in the SAB has not been investigated yet. In addition to these behaviors of the interface, chemical and hermetic sealing reliability is very important for the proper functioning of MEMS and microfluidic device packaging. However, a comparative study of the performance of the bonded interface created by SAB and SPAB has not been done yet.

This work reports on a systematic investigation of the performance of the silicon/silicon bonded interface fabricated by using SAB and SPAB. The bonding results include the bonding strength measured by tensile pulling tests, voids observed by infrared (IR) transmission images, and nanostructure of the interface performed by high resolution transmission electron microscopy (HRTEM) in different heating temperatures. Also, the hermetic sealing and chemical reliability of the interface has been reviewed.

2 Experimental Procedure

Commercially available one-side polished 50-, 100-, and 200-mm silicon (100) wafers were used. The thicknesses of the wafers were 275 ± 25, 525 ± 25, and 730 μm, respectively. The wafers were p-type and the resistivity was 20 to 30 $\Omega \cdot$cm. Rectangular cavities and microchannel structures were fabricated on the wafer-level samples by using the standard bulk micromachining processes.

In the SAB processes, a wafer-level robot-controlled SAB tool was utilized for the bonding experiments. It consists of a transfer chamber surrounded by processing, analyzing, heating, turning over/preliminary alignment (prealignment), alignment/preliminary bonding (prebonding), and bonding chambers. The tool is capable of eight wafers. The silicon wafers were loaded into the load lock chamber and then activated separately in the processing chamber by Ar-FAB with a voltage of 1.45 kV and 48 mA for 300 s unless otherwise mentioned. The background and process pressures were 1.4×10^{-9} and 4.2×10^{-4} Torr. More details of the SAB tool can be found in Ref. 2.

The sequential plasma activation of silicon surfaces was accomplished using newly developed hybrid plasma bonding (HPB), as shown in Fig. 2. The wafer-level HPB system consists of plasma activation and anodic bonding chambers. For this study, only a plasma activation chamber was used. The plasma activation chamber is equipped with reactive ion etching (RIE) and microwave (MW) plasma sources. The plasma activation chamber is separated into top and bottom compartments by an ion trapping metallic plate. The RIE and MW plasma were sequentially generated using O_2 and N_2 gases at the bottom and top compartments, respectively. The ion trapping metallic plate has 1-mm-diam holes, which trap charged ions. Therefore, MW plasma generates electrically neutral ions at the bottom compartment. The RIE and MW plasmas were generated at a frequency of 13.56 MHz and 2.45 GHz, respectively. Details of the sequential plasma activation can be found in Ref. 7.

The specimens of groups A and B show the plasma parameters to investigate the influence of O_2 RIE plasma time and power in the SPAB, respectively (Table 1). After plasma activation, the wafers were taken out of the chamber and

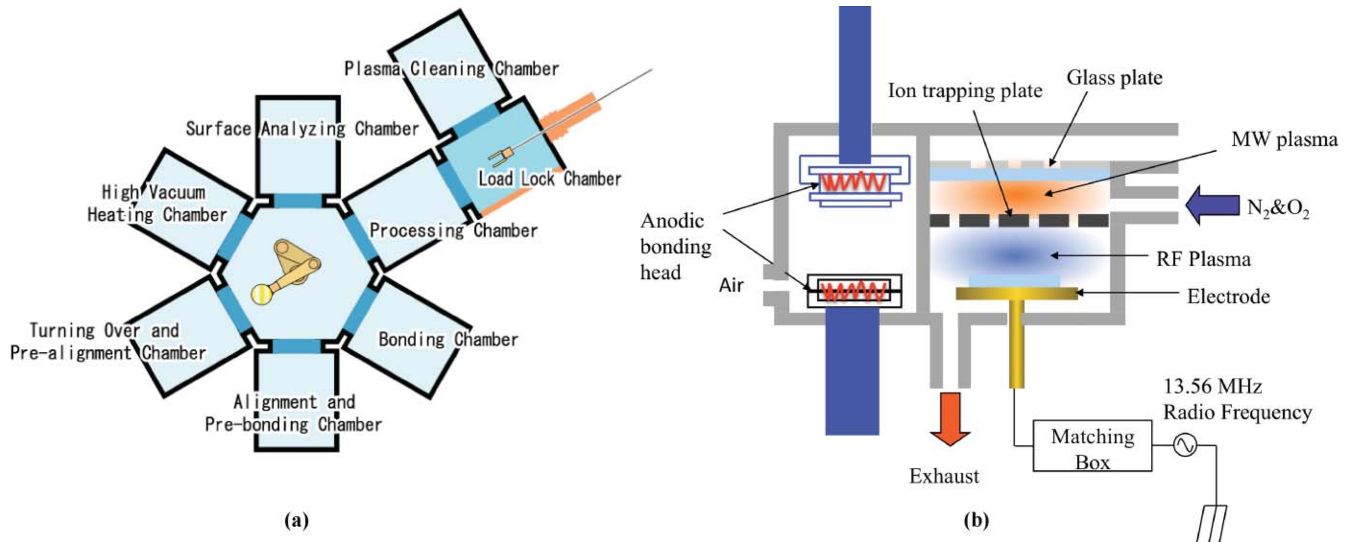

Fig. 2 Schematic diagram of the SAB, and hybrid plasma bonding (HPB) systems.[2,8]

bonded together by applying pressure manually. Finally, the bonded specimens were cold-rolled under 0.2-MPa pressure at room temperature to remove trapped air.

To investigate the influence of postbond annealing, the bonded specimens were annealed following a predefined annealing profile, which is discussed later. An infrared (IR) transmission method was used to investigate the voids in the silicon/silicon-bonded interface affected by different O_2 RIE times, powers, and annealing temperatures. For tensile strength measurements, the bonded specimens were diced into sizes of 10×10 mm. The diced pieces were glued with copper jigs, and the tensile strength was measured using an Instron (Norwood, Massachusetts) tensile tester. Specimens for HRTEM were prepared from the bonded pairs by standard procedures including dicing, polishing, dimpling, and ion milling. To investigate the elemental composition at the bonded interface, electron energy loss spectroscopy (EELS) was performed.

Table 1 Plasma parameters used for silicon surface activation.

	O_2 RIE plasma			N_2 MW radical		
Specimen number	Power (W)	Time (s)	Pressure (pa)	Power (W)	Time (s)	Pressure (pa)
A1		15				
A2	200	30	60	2500	30	60
A3		60				
B1	200					
B2	300	30	60	2500	15	60
B3	400					

3 Results and Discussion

3.1 *Annealing Effect on Bonding Strength*

In the SAB and SPAB methods, silicon wafers spontaneously bond on the activated surfaces without annealing.[10] On the other hand, hydrophilic bonding results from interaction between silanol (SiOH) groups formed on the surface, and requires annealing at high temperatures to achieve a bonding strength equivalent to that in the SPAB.[11,12] The bonding strength of silicon/silicon as a function of annealing temperature in the SAB and SPAB compared with the hydrophilic bonding methods is shown in Fig. 3.[13,14] The average bonding strength with standard deviation values are plotted for the SPAB method. In hydrophilic bonding, the bonding strength increased with the increase in annealing temperatures at different slopes. First, the bonding strength

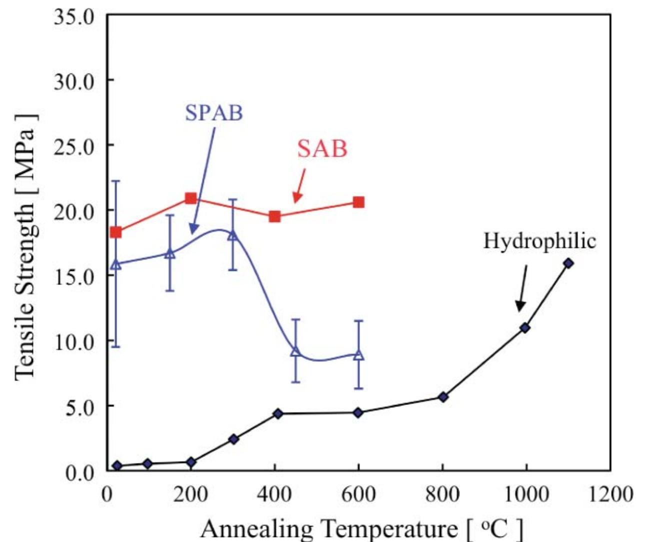

Fig. 3 Comparison of tensile strengths of silicon/silicon wafers in the SAB, SPAB, and hydrophilic bonding methods as a function of annealing temperature.[10,13,14]

monotonously changed from room temperature to 200°C, then it changed relatively with higher increasing rates up to 400°C. After that, it changed relatively with lower increasing rates up to 800°C, and finally increased with higher slope up to 1100°C. Before annealing, the bonding strengths of the specimens both in SAB and SPAB were higher than the bonding strength in hydrophilic bonding at 1100°C. After annealing up to 600°C, there is no significant influence on the bonding strengths in the SAB. In the SPAB methods, the bonding strengths increased with the increase in annealing temperature up to 300°C. After that, the bonding strengths decreased with the increase in annealing temperature. These characteristic differences in the bonding strength are attributed to the discrepant mechanisms of void nucleation relevant to the surface behavior across the interfaces. In previous studies, the rearrangement of water that causes void formation across the hydrophilic interface has been investigated.[12,15] Therefore, a comparative study of void nucleation in SAB and SPAB is investigated as a function of annealing temperature.

3.2 *Annealing Effect on Interfacial Voids*

To investigate the role of annealing on the nucleation of voids, the 50-mm Si/Si wafers bonded by the SAB method and 100-mm Si/Si wafers bonded by the SPAB method (B2, as shown in Table 1) were sequentially heated up to 600°C in air and nitrogen environments, respectively. The surface activation time was 60 s by Ar-FAB in the SAB. Before heating, the IR images were taken for the specimens. Then, the specimens were heated at 200, 400, and 600°C. The interfaces were observed after each heating step using an IR transmission camera. At all three temperatures, the 50-mm Si/Si wafers were heated for one hour with a ramping rate of 200°C per hour in air. For the specimen of B2, the heating time was four hours with a ramping rate of 200°C per hour in nitrogen environments with a nitrogen flow rate of 90 standard cubic centimeters per minute (sccm). Two typical examples of heating dependence of void evolution in SAB and SPAB are shown in Fig. 4[16] before heating and after heating at 600°C. In the SAB, thermal and plasma-induced voids were not observed. The white areas across the edge of the bonded interface are open areas due to blade tests. The void-free interface is in contrast to thermal and plasma-induced voids observed in the SPAB.

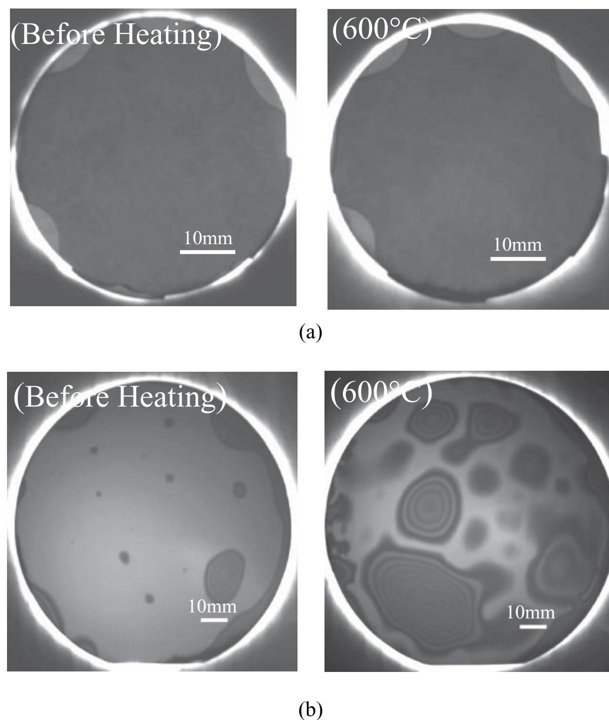

Fig. 4 IR transmission images of silicon/silicon interfacial voids prepared by (a) SAB and (b) SPAB before heating and after sequential heating at 600°C.[13,16]

In the SPAB, a considerable number of plasma-induced voids was observed before heating. The plasma-induced defect sites such as nanopores and craters were responsible for the voids.[16] After heating, the interfacial voids were not significantly changed up to 400°C in the SPAB. From 600°C, new voids appear due to thermal annealing (now termed thermal voids) with the presence of the original voids due to plasma processing (termed as plasma voids). In fact, the reduction of bonding strength at 450°C indicates that the thermal voids generate below 600°C (Fig. 3). The size and shape of the voids at the SPAB interface were increased with the increase in heating temperature. The size and shape of a few plasma voids were changed with a few Newton rings. The sizes of thermal voids were much bigger compared to that of the plasma voids. The nucleation of thermal voids is attributed to the generation of hydrogen gas from the oxidation reaction of silicon by the adsorbed water.[17] Voids become bubbles (bigger voids) by accumulating voids due to viscous flow of oxides above 400°C.[16] From 600°C, perfectly bonded regions surrounded the thermal voids. No transitions for void evolutions were observed after 600°C. Therefore, further annealing at higher temperatures neither generated the voids nor changed the size and shape. A comparison of the IR images at 600, 800, and 900°C[16] indicates that once the size and shape of the voids are defined at 600°C, they cannot be changed by thermal viscous flow because of high bonding strength at the surrounding areas of the voids already formed at 600°C. The nucleated sites of voids were mainly centered at the plasma-induced defect sites. The plasma-induced defects sites were responsible for the severe reduction of bonding strength for the specimens after heating.

3.3 *Annealing Effect on Nanointerface*

To correlate the transitions of macroscale voids with the nanometer scale interfacial behavior, HRTEM has been performed for the specimens before and after heating. Figure 5 shows the temperature dependence of HRTEM images of silicon/silicon bonded interfaces prepared by the SPAB and SAB. The SPAB specimens were sequentially heated. In both methods, an intermediate amorphous layer at the bonded interface was observed. In the SPAB, the thickness of the interfacial amorphous layer thickness was ∼4.8 nm before heating. After heating, while the amorphous layer thickness remained constant after heating at 200 and 400°C, it increased to 13-nm thickness after heating at 600°C. The sudden increase in the amorphous layer at 600°C can be correlated with the sudden increase in void density observed from IR

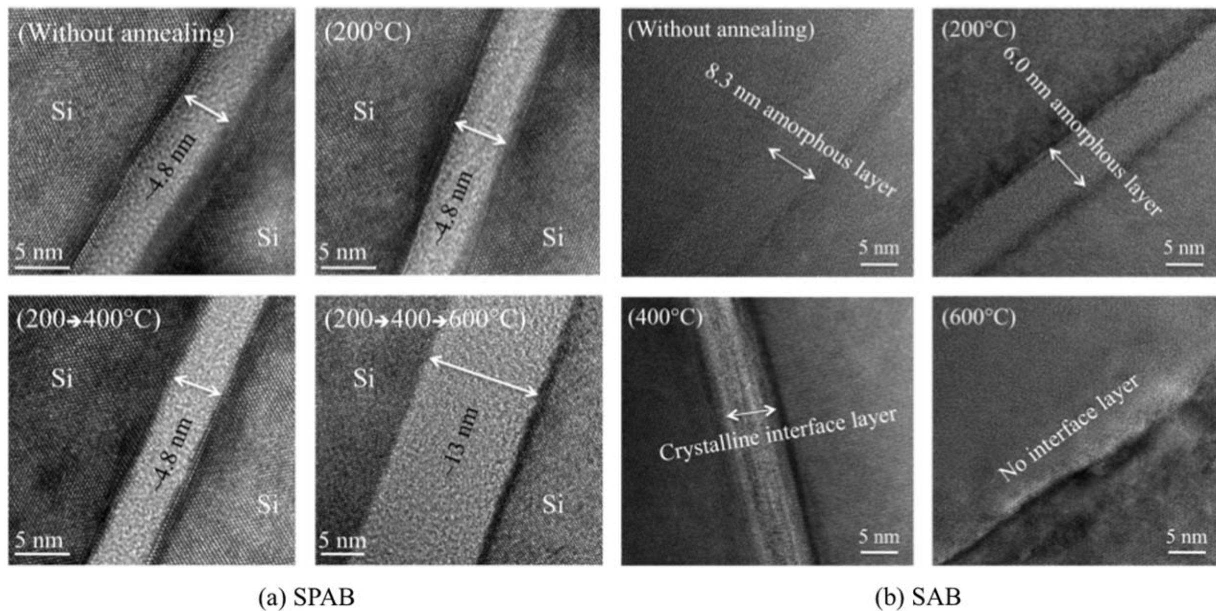

Fig. 5 HRTEM images of silicon/silicon interfaces in (a) SPAB and (b) SAB before heating and after heating up to 600°C. In SPAB, the specimens were sequentially heated.[8,13]

transmission images.[16] This is caused by: 1. the breaking of SiO_xN_y, and 2. viscous flow of H_2 gas generated from adsorbed H_2O from bulk silicon.[8] In addition, high concentration of oxygen interstitials in CZ silicon[10] can be responsible for the increased thickness. Due to small amount of SiO_xN_y at the interface, the abrupt change in amorphous layer thickness can be correlated with the oxidation of silicon by the absorbed water onto the plasma-activated silicon surfaces as follows:

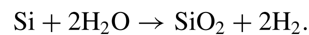

$$Si + 2H_2O \rightarrow SiO_2 + 2H_2.$$

Therefore, the reaction product SiO_2 is responsible for the abrupt change in amorphous layer thickness, and reaction byproduct H_2 is responsible for the nucleation of thermal voids across the interface at 600°C.

In the SAB, the thickness of the interfacial amorphous layer thickness was ~8.3 nm before heating. After heating at 200°C, the amorphous layer was decreased to ~6.0 nm. After heating at 400 and 600°C, the amorphous layer was diminished. This behavior is in contrast to that in the SPAB because of the absence of trapped air/oxides at the interface in the SAB.

3.4 *Nanointerfacial Behavior at Low Temperature (50 to 225°C) Annealing*

In the SPAB, although the thermal voids were insignificant up to 400°C, the rearrangement of OH molecules at the interface as well as their reactions with silicon would happen. To clarify the role of diffusion of OH molecules from the interface into bulk silicon on the bonding strength in the SPAB, the silicon/silicon interface has been extensively investigated after annealing at low temperatures. Figure 6 shows the HRTEM interface images of a specimen, treated with identical plasma parameters of the specimen A3, except the O_2 RIE power (50 W) and pressure (50 Pa), after annealing at 50, 100, 150, and 225°C for 1 h in air.[18] The HRTEM images showed intermediate amorphous layers across all the interfaces. The thicknesses of the amorphous layer after annealing at 50, 100, 150, and 225°C were 3.8, 3.4, 2.8, and 3.3 nm, respectively. The decrease in the thickness of the amorphous layer from 50 to 150°C indicates absorption of hydroxyl molecules from the interface to the bulk of silicon. In contrast to the absorption behavior at 150°C, the increase in the

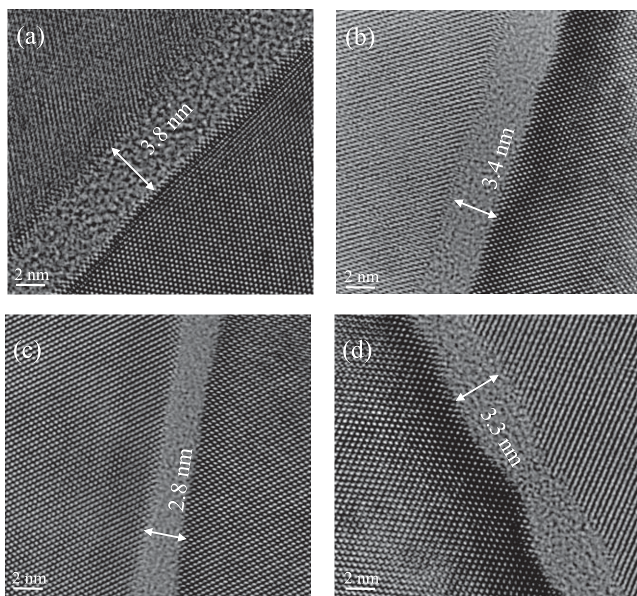

Fig. 6 HRTEM images of the Si/Si interfaces created by SPAB that were annealed at (a) 50, (b) 100, (c) 150, and (d) 225°C for 1 h in air. The sequential activation consists of a 50-W oxygen RIE plasma with time of 60 s at 50 Pa and a 2500-W MW nitrogen radical with time of 30 s at 60 Pa.[18]

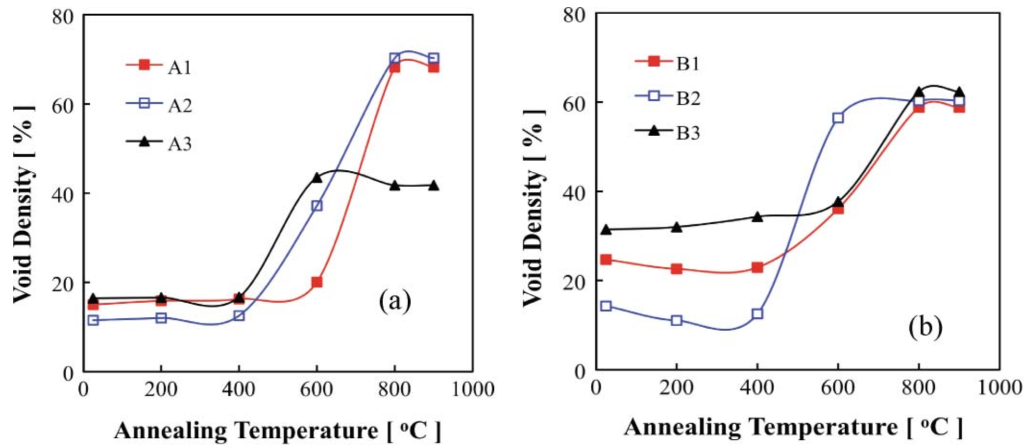

Fig. 7 Void density in the SPAB for (a) O_2 RIE time-dependent specimens (Al, A2, A3) annealed in air, and (b) O_2 RIE power-dependent specimens (Bl, B2, B3) annealed in nitrogen gas for 4 h at each step.[16]

thickness of the amorphous layer was observed at 225°C. This is due to the desorption of hydroxyl molecules from the bulk of silicon to the interface. The annealing at 225°C starts producing hillocks at the interface that turn into thermal voids at higher temperatures to absorb the gas produced from the desorbed water at the interface.

3.5 *Quantitative Analysis of Voids from Room Temperature to 900°C*

As previously seen, the thermal voids were grown preferentially at plasma-induced defect sites on the activated surfaces. Therefore, the investigation of the void density associated with their transitions offers insight to the nucleated voids. Figure 7 shows the quantitative analysis of void density in the SPAB for O_2 RIE time-dependent specimens (Al, A2, A3) annealed in air [Fig. 7(a)], and O_2 RIE power-dependent specimens (Bl, B2, B3) annealed in nitrogen gas as a function of annealing temperatures [Fig. 7(b)].[16] Table 1 shows the plasma parameters used for the silicon surface activation for SPAB. The void density was estimated from the IR images on scaled paper. A few percents of discrepancy may exist in the estimation of the void density due to human errors. While the plasma void density remained constant up to 400°C, the thermal void density was suddenly increased for all the specimens at 600°C, except for the specimen (B3) treated with an O_2 RIE power of 400 W in nitrogen. For the B3 specimen, thermal void nucleation started at 800°C. Below 400°C, the void density for the specimens [Fig. 7(b)] annealed in N_2 gas was higher than that of the specimens [Fig. 7(a)] annealed in air. Above 600°C, the amount of thermal void density in the O_2 RIE time-dependent behavior for specimens Al and A2 was higher compared with that of the Bl, B2, and B3 specimens treated with RIE power. This higher amount of void density was caused by higher activation time of N_2 radical (30 s) for specimens Al and A2. The O_2 RIE plasma activation times for Al and A2 were 15 and 30 s, respectively, that were not sufficient to remove native oxides and surface particles from the silicon surface. These remaining native oxides and surface particles worked as precursors for the enlargement of the voids. On the other hand, specimen A3 treated for 60 s had lower saturated void density at and above 600°C. This is attributed to the higher removal of native oxides and higher oxide thickness due to the prolonged surface activation.[19,20]

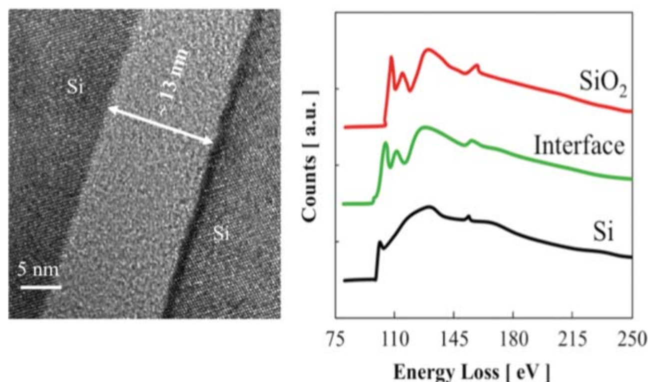

Fig. 8 Compositional distribution by EELS analysis (right) across the silicon/silicon interface (left) after sequential heating at 600°C.[8,16]

The characteristic behavior of the temperature-dependent void density can be used to explain the bonding strength as a function of temperature in the SPAB of Fig. 3. A comparison between Figs. 3 and 7 showed that the bonding strength up to 400°C did not change because there was no gas formation across the interface. After that, the bonding strength was reduced due to the increased amount of voids across the interface. Similar behavior of the influence of voids on bonding strength has been reported.[15]

3.6 *Nanointerfacial Behavior at High Temperature Annealing*

To investigate the elemental composition at the bonded interface after annealing, EELS was performed with the SPAB specimen sequentially heated at 600°C, shown in Fig. 8(b). The EELS experiment was performed using a field-emission TEM [JEOL (Tokyo, Japan) 2100F, $C_s = 0.50$ mm] in conjunction with a Gatan Enfina (Pleasanton, California) 1000 spectrometer operating at 200 kV. The energy resolution was about 1.0 eV and a 1.0-nm-diam probe was used. Core-loss EELS spectra of N-K, Si-$L_{2,3}$, and O-K were recorded.

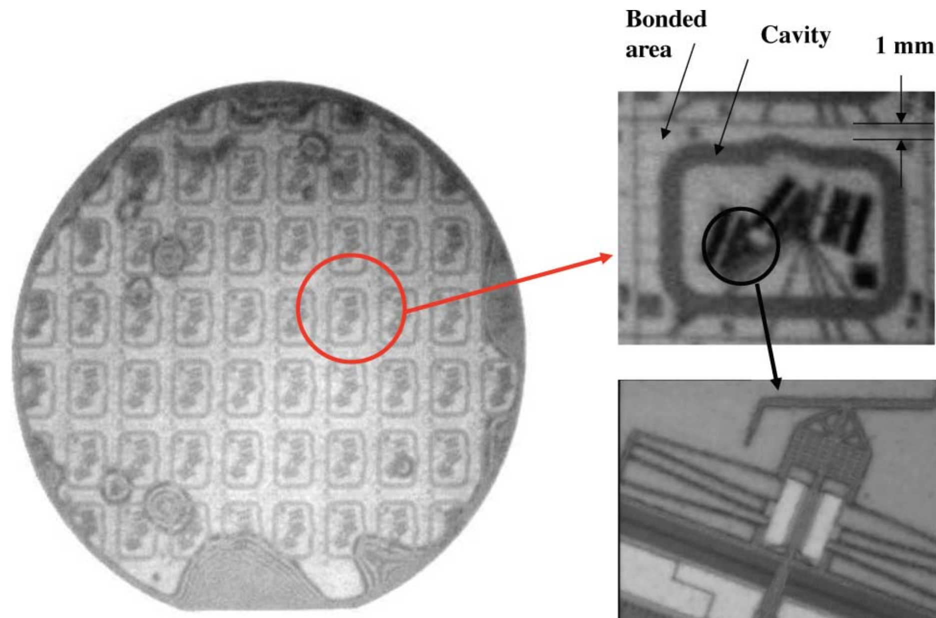

Fig. 9 IR transmission image of whole bonded area (left) and a cell (right) with selected area of bare silicon bonded with MEMS and microfluidic structured silicon after cleaning with a low-energy Ar ion source at room temperature.[1]

From the EELS spectra, no nitrogen was detected at the bonded interface. The Si- $L_{2,3}$ edges of the 125 to 175 eV and the O-K edges at 540 to 560 eV were observed at the amorphous interface layer. To investigate the characteristic behavior of the amorphous interface layer, the Si- $L_{2,3}$ edges of the amorphous interface layer were compared with that of standard Si and SiO_2, as shown in Fig. 8. The Si- $L_{2,3}$ edges from the amorphous interface layer were identical to those of the standard SiO_2. Thus, the presence of SiO_2 at the interface is confirmed. This is because of the oxidation of sequentially annealed silicon at 200, 400, and 600°C for 4 h at each step in air.

4 Applications of Surface-Activated Bonding and Sequentially Plasma-Activated Bonding in Microelectromechanical Devices and Microfluidics

4.1 *Sealing of Microelectromechanical Devices*

Packaging of complicated MEMS and microfluidic structures for lab-on-a chip applications, for example, requires bonding for substrates with silicon and silicon oxide on the same surface. The influence of silicon and silicon oxide on the same surface on the bonding quality with silicon has been investigated (Fig. 9). Although the etching rates of silicon (0.08 nm/s) and SiO_2 (0.06 nm/s) are different, there was no influence of the presence of oxide and nonoxide structures on the bonding quality. The IR images show that the silicon oxides isolate microstructures from each other. The bonding experiment utilized the SAB using an Ar low-energy ion beam with 80 eV and 3 A at a background pressure of 10^{-6} Pa for 60 s. The external pressure for bonding in the SAB is 0.2 MPa. The average bonding strength was above 10 MPa. The low activation time resulted in strong bonding of these complicated structures with silicon.

To investigate the applicability of SAB and SPAB, the leak test and hermetic sealing behavior have been investigated. Figure 10(a) shows the leak test for silicon/glass cavities. Silicon with cavities of sizes $5.6\times2.4\times0.04$ to 0.09 mm was bonded with bare glass wafers using the SPAB. The bonded wafers were diced into chips of sizes 13×13 mm for the radioisotope fine leak test. The horizontal and vertical sealed widths of the cavity were 3.3 and 1.7 mm, respectively. The whole chip area with the cavity was 9×9 mm^2. A number of eight sealed cavities was exposed to a mixture of krypton-85 gas of specific radioactivity of 1.6×10^{12} Bq/m^3 in a background high pressure of 5×10^5 Pa for 15 h to measure the leak rate of the cavities. The leak rate L (atm cc/s) of the exposed cavities was measured outside the chamber by measuring radiation counts coming out of the cavities using a scintillation counter. The leak rate can be estimated using the equation $L = R/sKTP^2$, where R is the counts per min above ambient background, s is the specific activity of Kr gas (ci/atmcc), k is the counting efficiency of the scintillation crystal, T is the soak time (s), and P is the applied pressure (atm). The background dose was 71 to 95 cpm. The estimated leak rate was lower than 1.0×1.0^{-9} Pa $\cdot$ m^3/s, which satisfies the requirements for Military Standards (MIL-STD)-883E encapsulation standard in hazard environments.[2,7]

On the other hand, vacuum seal behavior of the cavity created by the SAB was examined by the measurements of quality factor of the cavity as a function of chamber pressure [Fig. 10(c)]. The quality factor (vibration characteristics) of a damped system can be defined by $Q = 2\pi U_i/U_d$, where U_i is the stored vibration energy and U_d is the dissipated energy per period. The vacuum seal cavity was fabricated in the following. First, a Pyrex glass wafer was bonded to silicon dioxide on a silicon wafer by anodic bonding. Then cavities were fabricated on the silicon side using anisotropic tetramethylammonium hydroxide (TMAH) etching. Chips with cavities of $5.6\times2.4\times5$ mm^3 were diced from

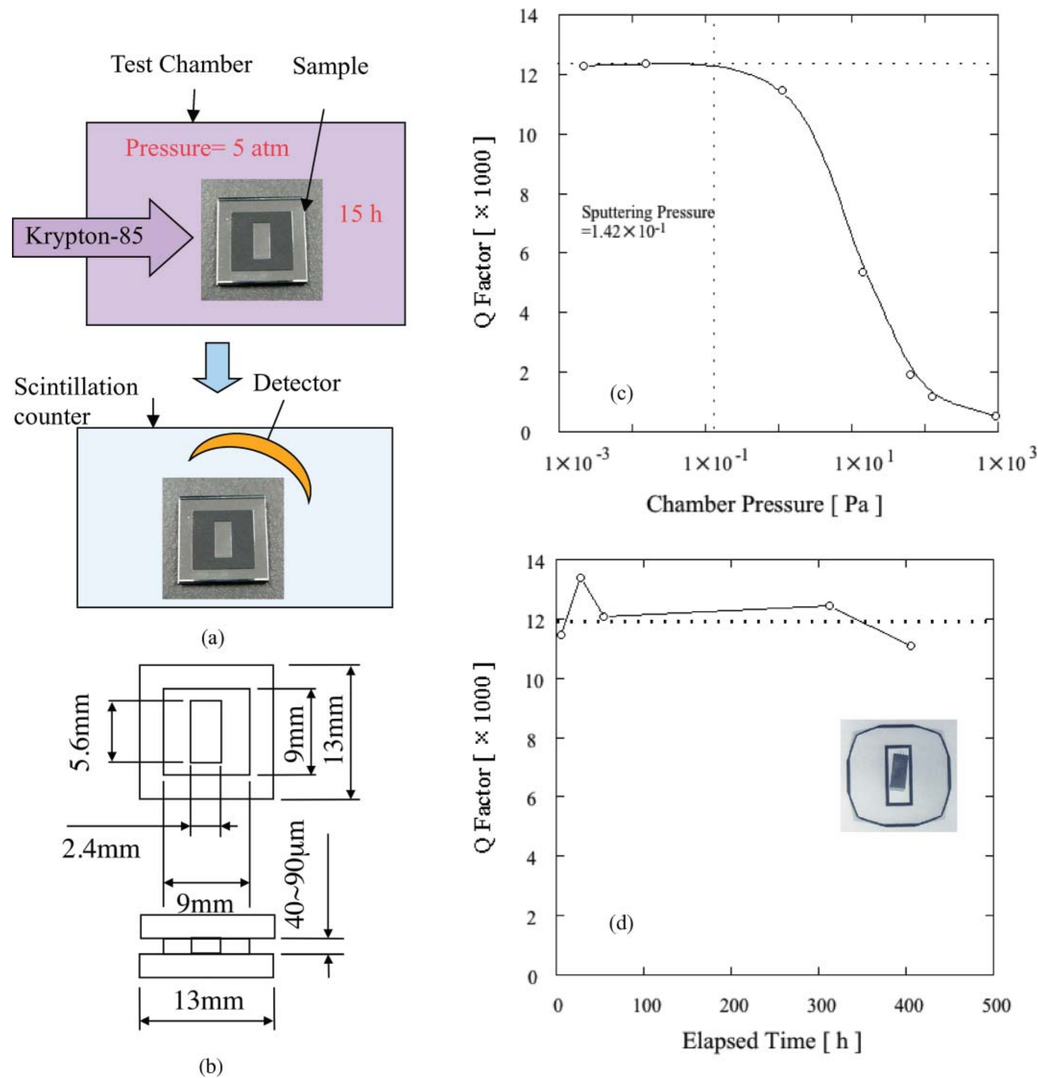

Fig. 10 (a) Schematic for radioisotope fine leak test. (b) Dimension of the bonded chip. (c) Pressure and (d) time dependence on the Q factor measured in an atomic force microscope.[2]

the fabricated silicon/glass wafers. Then a microcantilever of 33-kHz resonant frequency was placed in the cavity structure and fixed on glass with indium paste to measure Q values of the cavities. The size of the cantilever was $300 \times 35 \times 2\ \mu m^3$. Finally, the cavities with the cantilever were bonded with silicon (i.e., bonding between silicon and silicon). The activation energy and current were 1.5 keV and 15 mA, respectively. The activation was accomplished simultaneously using two Ar-FAB sources with 45-deg incident angles in a UHV single chamber. The time dependence of Q values of the sealed cavities was measured by using an atomic force microscope (AFM, Seiko Instruments, Incorporated, Austin, Texas, SPI3800N) [Fig. 10(d)]. The quality factor of the cavity was compared with that of the AFM vacuum chamber. The Q-dependent chamber pressure was measured using a similar cantilever in the AFM chamber [Fig. 10(c)]. The quality factors were measured through the laser beam deflection of the cantilever beams of the AFM both in the sealed cavities and AFM vacuum chamber. The quality factor of both the cavity and AFM vacuum chamber corresponds to the vacuum pressure inside the cavity. Identical Q values at the reference vacuum level at the time of surface activation and cavities were observed. This is indicative of air-tight cavities. However, the leak rate (∼quantity of air in cubic meters flowing through a leak per second) of the vacuum-sealed cavities was estimated from the difference between the maximum and minimum Q values and the cavity volume (cantilever volume was deducted). The estimated leak rate was 2.6×10^{-16} Pa m^3/s after 400 h, which was much lower than the American MIL STD for hermetic sealing in hazardous environments.

4.2 *Reliability in Microfluidics*

Figures 11(a) and 11(b) show the IR images of a whole 4-in. wafer and two cavities out of 180 in a cell, respectively. Figure 11(c) shows the cross sectional scanning electron microscope (SEM) image of the bonded interface. The wafer has a total number of 46 cells. Each cell has 180 cavities. Each cavity has 11.5-mm-long, 180-μm-deep, and 20-μm-wide channels. The space between two bonded channels is 40 μm. After the fabrication of deep channels, a 20-μm-thick

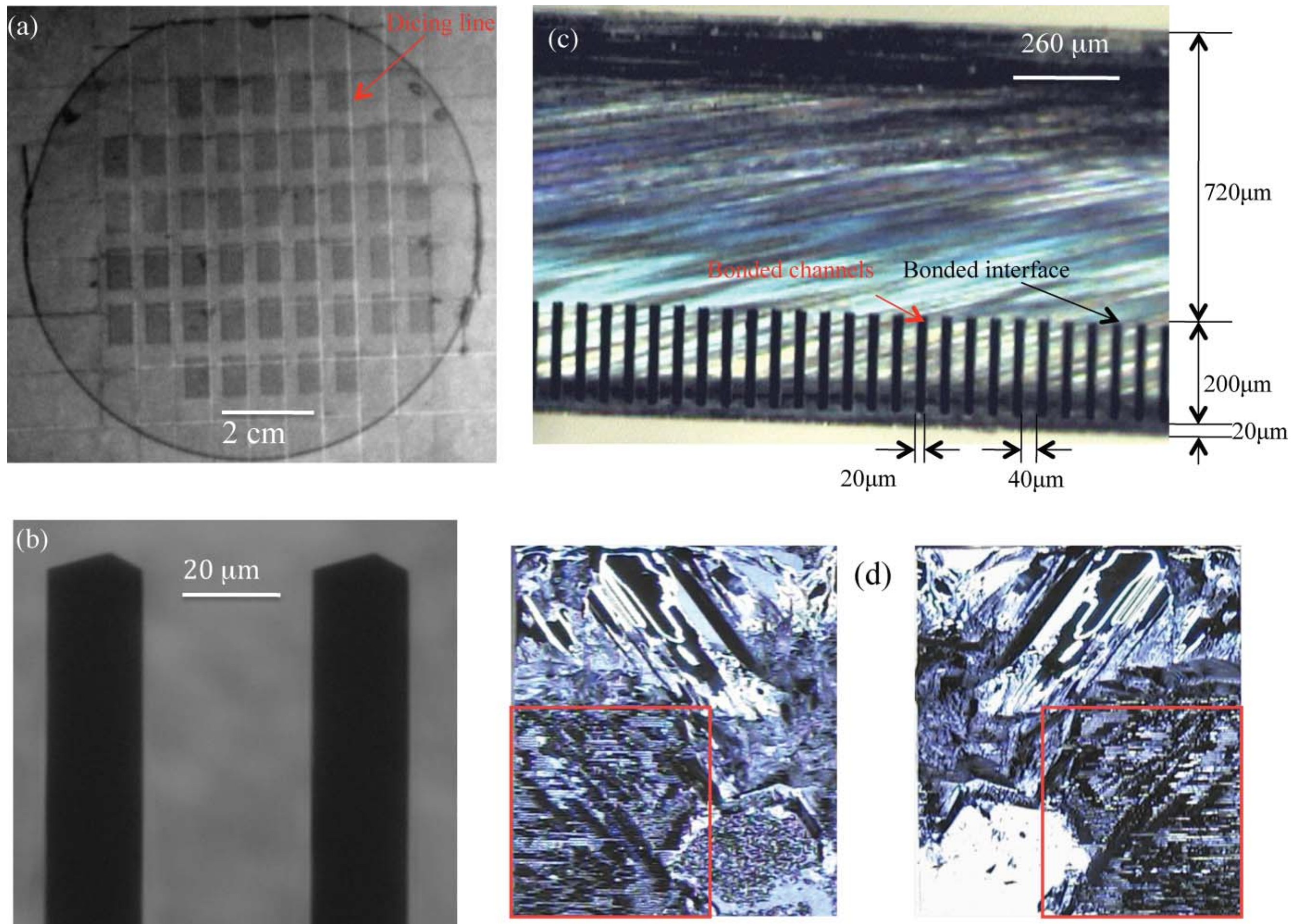

Fig. 11 Images of microfluidic channels in silicon after bonding with bare silicon. (a) IR image of the whole bonded interface. (b) IR image of two cavities out of 180 in a cell. (c) Cross sectional scanning electron microscope (SEM) image of the bonded interface. (d) Fracture images of the bonded interface after tensile pulling tests.[21]

silicon layer is left after making the channels on a 200-μm-thick silicon wafer. The dicing places are seen on the bonded area as white lines. The IR images of the cell areas are black because of the sealed channels in the cell. No visible voids were seen across the bonding interface among fine channels [Figs. 11(a) and 11(b)]. Figure 11(d) shows the fracture images of the bonded interfaces of bare/microfluidic structure wafers after tensile pulling tests.[21] The marked area is the bonding area with fine patterns and the rest is a bare bonded area. The fracture images show bulk fractures both in bare and patterned regions. The bonded interface can be useful for microfluidic channels and reservoir applications where micro/nanoliters[1] of liquid may be required and externally pumped with strong pressure into the working area.

For chemical reliability observation, the bonding strength of the silicon/silicon interfaces prepared by the SAB and SPAB after dipping in water, ethanol, acetone, and 3% HF for 30 days at room temperature has been measured, as shown in Fig. 12(a). Three bars represent the data for three specimens. The bonding strength showed considerable dependence on the chemical types. The bonding strength in the SPAB was higher than that in the SAB, except for dipping in HF. The bonding strength in the SPAB was not noticeably degraded in HF. The considerable difference in the bonding strength of the SAB and plasma-processed interfaces dipped in HF was controlled by different chemical compositions at the interfaces.

Figure 12(b) shows the bonding strength of silicon/silicon bonded interfaces in the SAB and SPAB at room temperature as a function of dipping time in 3% HF acid. The bonding strength decreased with the increase of HF dip time. The bonding strength for SAB-processed interfaces remained constant for 20 days. In the SAB, silicon wafers were activated with an Ar low-energy ion source of 80 V and 3 A for 10 s, and bonded in a vacuum pressure of 10^{-7} Pa. In the SPAB, the wafers were activated with O_2 RIE and N_2 radicals each for 60 s and bonded under hand-applied pressure. In the SAB, the bonding strength remained constant for 20 days and then decreased with the increase of dipping time. In the SPAB, the bonding strength decreased in the increase of dipping time from the beginning of the experiments. This time-dependent discrepant behavior can be explained using the chemical compositions across the interface. Faster decrease of the silicon/silicon bonding strength in the SPAB was due to the etching of oxides and the presence of voids across the interface. On the other hand, such oxides are not present in the SAB, and resulted in lesser etching than the SPAB interface.

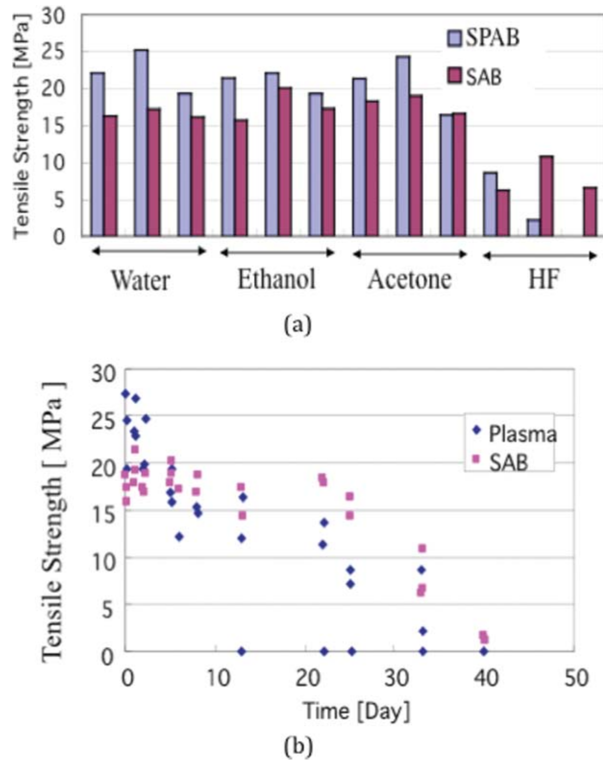

Fig. 12 (a) Bonding strength of silicon/silicon as a function of dipping in (a) various chemicals and (b) time in 3% hydrofluoric acid at room temperature.[7]

5 Conclusions

A comprehensive review of surface-activated bonding (SAB) compared with sequentially plasma-activated bonding (SPAB) is given with applications for packaging microelectromechanical systems (MEMS) and microfluidic devices. The bonding strength of the interface in the SAB and SPAB is as high as that of conventional hydrophilic bonding methods, which require annealing as high as 1000°C to achieve covalent bonding. Before heating, while a void-free interface is achieved in SAB, a considerable number of voids are observed in the SPAB, which is due to the plasma-induced surface defects. After heating, voids are not observed and bonding strengths are not changed in the SAB. On the other hand, increase in interfacial voids with annealing temperatures is observed, which decreases the bonding strength in the SPAB. Although the rearrangement of water such as absorption and desorption across the bonded interface is found below 225°C, the voids are not significant up to 400°C. Annealing above 600°C results in a considerable amount of thermal voids due to the viscous flow of oxides. Amorphous layers with thicknesses of 8.3 and 4.6 nm are observed at interfaces in the SAB and SPAB, respectively, before heating. These disappear and enlarge in SAB and SPAB, respectively, after heating. Electron energy loss spectroscopy shows the presence of SiO_2 in the nanointerfacial amorphous layer due to oxidation of the silicon/silicon interface after sequential heating. The bonding strength, sealing, and chemical performances of the interfaces meet the requirements for microelectromechanical systems and microfluidics applications.

Acknowledgments

This research was supported by a discovery grant (number 327947) from the Natural Science and Engineering Research Council of Canada, and an infrastructure grant (number 12128) from the Canada Foundation for Innovation (CFI). Jamal Deen is greatly thanked for his support and assistance in establishing nanobonding and interconnection research at the Micro- and Nano-Systems Laboratory at McMaster University. Moon J. Kim from the University of Texas at Dallas is thanked for the contribution in the high resolution transmission electron microscopy experiments. Fangfang Zhang and M. G. Kibria are greatly acknowledged for their assistance in the preparation of the manuscript.

References

1. M. M. R. Howlader and T. Suga, *Proc. Electron. Comp. Technol. Conf.*, pp. 1423–1429 (2009).
2. M. M. R. Howlader, H. Okada, T. H. Kim, T. Itoh, and T. Suga, *J. Electrochem. Soc.* **151**(7), G461–G467 (2004).
3. S. H. Choa, *Microelectron. Reliab.* **45**, 361–369 (2005).
4. T. Itoh and T. Suga, *J. Micromech. Microeng.* **15**, S281–S285 (2005).
5. W. B. Yu, C. M. Tan, J. Wei, S. S. Deng, and S. M. L. Nai, *Sens. Actuators A* **115**, 67–72 (2004).
6. S. C. Johnston, *Semicon. Int.* **30**(1), 34 (2007).
7. M. M. R. Howlader, S. Suehara, H. Takagi, T. H. Kim, R. Maeda, and T. Suga, *IEEE Trans. Adv. Packag.* **29**, 448–456 (2006).
8. M. G. Kibria, F. Zhang, T. H. Lee, M. J. Kim, and M. M. R. Howlader, *Nanotechnol.* **21**(13), 134011 (2009).
9. M. Bruel, *Nucl. Instr. Meth. Phys. Res. B* **108**, 313 (1996).
10. M. M. R. Howlader, T. Suga, H. Itoh, T. H. Lee, and M. J. Kim, *J. Electrochem. Soc.* **156**, H846–H851 (2009).
11. M. M. R. Howlader, T. Suga, H. Itoh, and M. J. Kim, *ECS Trans.* **3**, 191–202 (2006).
12. Q. Y. Tong and U. Gosele, *Semiconductor Wafer Bonding*, p. 52, Wiley, New York (1999).
13. M. M. R. Howlader, M. G. Kibria, and F. Zhang, *Thin Solid Films* (in press).
14. M. Shimbo, K. Furukawa, K. Fukuda, and K. Tanzawa, *J. Appl. Phys.* **60**(8), 2987–2989 (1986).
15. X. X. Zhang and J. P. Raskin, *J. Microelectromech. Sys.* **14**, 368–382 (2005).
16. M. M. R. Howlader, F. Zhang, and M. G. Kibria, *J. Micromech. Microeng.* **20**(6), 065012 (2010).
17. M. Eichler, B. Michel, M. Thomas, M. Gabriel, and C. P. Klages, *Surf. Coat. Technol.* **203**, 826–829 (2008).
18. M. M. R. Howlader, G. Kagami, T. H. Lee, J. G. Wang, M. J. Kim, and A. Yamauchi, *J. Microelectromech. Syst.* **19**(4), 840–848 (2010).
19. V. Dragoi, G. Mittendorfer, C. Thanner, and P. Lindner, *Microsystem Tech.* **14**, 509–515 (2008).
20. M. Eichler, B. Michel, P. Hennecke, and C. P. Klages, *J. Electrochem. Soc.* **156**, H786–H793 (2009).
21. D. Pasquariello, C. Hedlund, and K. Hijort, *J. Electrochem. Soc.* **147**(7), 2699–2703 (2000).
22. S. Bengtsson and P. Amirfeiz, *J. Electron. Mat.* **29**, 909–915 (2000).
23. A. Weinert, P. Amirfeiz, and S. Bengtsson, *Sens. Actuat. A* **A92**, 214–222 (2001).
24. C. Yang, U. Tartaglino, and B. N. J. Persson, *Phys. Rev. Lett.* **97**, 116103–11604 (2006).
25. X. Ma, C. Chen, W. Liu, X. Liu, X. Du, Z. Song, and C. Lin, *J. Electrochem. Soc.* **156**, H307–H310 (2009).

Dr. Matiar M. R. Howlader received the BScEng degree in electrical and electronic engineering from Khulna University of Engineering and Technology, Khulna, Bangladesh, in 1988, and the MS and PhD degrees in nuclear engineering from Kyushu University, Fukuoka, Japan, in 1996 and 1999, respectively. From 2000 to 2005, he was with the Research Center for Advanced Science and Technology, The University of Tokyo, Japan, as an endowed associate professor. He is currently an assistant professor in the Department of Electrical and Computer Engineering, McMaster University, Hamilton, Ontario, Canada. His research focuses on chip-size and wafer-level planar and vertical integration for microelectronics, microelectromechanical systems, and optoelectronics packaging, oxidation behavior of solders and electronic materials, interfacial adhesions, and radiation effects on materials and packages. He has started a new initiative on nanobonding and packaging of materials, devices, and components for microsystems and nanosystems for health and environmental applications. He has published more than 40 refereed papers and more than 65 international proceedings articles. He is a member of the Japan Institute of Electronic Packaging. He was the recipient of the Best Technical Paper Award at the International Conference on Electronic Packaging in 2003.

Tadatomo Suga received the MS degree in precision engineering from the University of Tokyo in 1979. He joined the Max-Planck Institut für Metallforschung, Stuttgart, in 1979, and received the PhD degree from the University of Stuttgart in 1983 for his study on fracture mechanics characterization of metal-ceramic interfaces. In 1984 he became a member of the Faculty of Engineering at the University of Tokyo, and since 1993, he has been a professor of precision engineering. He is also conducting a research group at the National Institute of Materials Science (NIMS) in Tsukuba as a director, and he is a member of the Science Council of Japan. His research focuses on microsystems integration and packaging, and development of interconnect technology, especially room temperature bonding techniques for various applications. He has published 200 papers and five books in the field of material science and electronic packaging.

Queries

Q1: Au: Please provide article titles for all references.
Q2: Au: Update for Ref. 13.
Q3: Au: Refs. 22–25 are not cited in text (old Refs. 16, 17, 23 and 24). Please place in text in order or delete.